Supporting Information

Vollmer et al. 10.1073/pnas.1408206111

NanoSIMS Analysis

It is well established from bulk isotopic measurements, mineralogical features, volatile contents, and other characteristics that organic materials in Renazzo-type (CR) chondrites are among the most primitive available for study (e.g., refs. 1 and 2). Antarctic Graves Nunataks (GRA) 95229 contains abundant and highly diverse organic materials (3, 4), and Northwest Africa (NWA) 852 has been shown to host anomalous organic ^{15}N-rich grains despite the extensive aqueous alteration that has destroyed most of the presolar silicate stardust (5). Interplanetary dust particles (IDPs) are collected in the stratosphere, generally of low density and fine grained, and mostly <50 μm in diameter. They are well known for their pristine components and presumably originate mostly from comets (e.g., refs. 6–10). Isotopically anomalous hot spots were detected by standard ion imaging techniques with the Cameca NanoSIMS ion probes (11) at the Carnegie Institution of Washington, DC, and the Max Planck Institut für Chemie in Mainz, Germany. This high spatial resolution ion probe uses a finely focused Cs^+ primary beam to sputter negative secondary ions of H and D, ^{12}C and ^{13}C, or ^{12}C^{14}N and ^{12}C^{15}N together with reference isotopes (^{16}O and/or ^{28}Si) in multicollection mode. The ions sputtered from each position are detected in a double-focusing mass separator and converted to digitized ion images for each species. In calculated isotope ratio images, isotopically anomalous hot spots can be easily identified (Figs. S1–S4), and their ratios can be quantified with percent precision. Isotopic ratios of detected regions of interest are reported as δ values, which are deviations from the terrestrial standard in ‰ units. Details of the analytical procedure can be found elsewhere (e.g., ref. 10).

All isotopic compositions reported here and in the literature are usually related to terrestrial compositions, i.e., the terrestrial atmosphere in the case of nitrogen and the terrestrial water in the case of hydrogen (Standard Mean Ocean Water). We now know from the results of NASA's Genesis mission that the Sun is depleted in ^{15}N relative to the terrestrial atmosphere by ∼380‰ (12). Anomalous hot spots of the kind discussed here are then even more anomalous compared with the Sun.

Scanning Electron Microscopy

Following NanoSIMS analysis, isotope hot spots were then relocated in a high-resolution scanning electron microscope (SEM) at the University of Manchester and the MPI in Mainz by comparing NanoSIMS ion images with the same areas in the SEM. As these hot spots of organic matter can be relatively large (up to 760 nm in this work) and may also stand out in secondary electron images by their darker contrast, they can be usually well distinguished from surrounding silicates, metal grains, and sulfides (Figs. S1–S4). The selection of relatively large organic grains for transmission electron microscopy (TEM) analysis may introduce a bias for inferred characteristics of organics. This is a typical problem for combined SIMS–TEM work because only large enough grains are usually chosen for focused ion beam (FIB) preparation. Furthermore, the areas scanned for isotopic hotspots in both CR chondrites and IDPs are vastly different because IDPs are much smaller than matrix areas in meteorites. This may introduce a sampling bias in our dataset as well.

FIB Preparation

FIB preparations were performed on two different instruments: the two grains from GRA 95229 were prepared on a Zeiss CrossBeam EsB 1540 at the University of Münster, and the remaining grains were prepared on an FEI Helios NanoLab at the Institute for Functional Materials of the University of Saarbrücken (Germany). To improve reidentification of targeted grains in later TEM analyses, a dedicated marking protocol was applied (13), where a small e-beam–deposited Pt cap is put on top of the areas of interest and a row of holes is shot into the surrounding material along the final line of thinning (Figs. S1–S4). Because organic matter is very prone to electron beam damage (14), electron beam exposure times of the grains in the final lamellae were reduced to a minimal amount. However, because FIB is a preparation technique which may induce artifacts into the final lamellae (e.g., amorphization, structural reorganization, and chemical modification), we cannot entirely exclude that some grains of interest may have been affected. As the relative inelastic mean free path (mfp) of electrons at the lower acceleration voltages as used by SuperSTEM increases compared with traditional high-voltage instruments (15), we thinned the sample down to less than 100 nm. In later EELS analyses, thicknesses of respective areas using the EELS-log-ratio technique (15) were around 1–1.5 mfp units (at 60 kV). During preparation of the FIB sections, some material from the grains was lost. The globular morphology of grain 13_4 can still be identified, but only two small patches remained intact for analysis (Fig. S2). The same is true for grain 14_2, where a small area of carbonaceous material was left on the bottom of the initial grain, protected from sputtering by higher Z material (Pt from the preparation) lying on top of it (Fig. S2). Material was also lost from the IDP organic grains, and we cannot be totally sure that the lamellae contain the anomalous grains of interest because organic grains are very small (Table S2). Still, we are confident that the measured carbonaceous grains are genetically connected to the isotopically anomalous grains of interest. EEL spectra of the IDP organic grains could still be recorded successfully (Fig. S5).

UltraSTEM Investigations

Prepared lamellae were intentionally not documented previously in a conventional (200 kV) TEM before the measurements at the SuperSTEM Laboratory in Daresbury (UK) to avoid potential damage or contamination of the sample. We used a dedicated C_s-(spherical aberration coefficient) corrected Nion UltraSTEM 100 for sample analysis operating at 60 kV in gentle STEM conditions (16). Because this acceleration voltage is below the knock-on threshold for carbon (∼80 kV), any damage to the regions of interest by these effects could be eliminated. The probe current (down to below 10pA in the most sensitive samples) and dwell times (fast scanning times and cumulative imaging at low dose rates) were further tailored to obtain electron doses low enough to avoid any observable beam damage. The vacuum system allows for near–ultrahigh-vacuum conditions near the specimen, thus preventing sample contamination through spurious carbon buildup or chemical etching due to residual gases in the column. The instrument is equipped with a cold field emission electron source with a nominal energy spread of around 0.3 eV, a quadrupole-octupole C_s-corrector in the condenser system allowing for correction of up to sixfold astigmatism and sub-Ångstrom resolution, an ultrastable stage, conventional bright-field (BF) and high-angle annular darkfield (HAADF) detectors, and a Gatan Enfina EEL spectrometer. The probe forming optics were adjusted to provide a 0.11-nm probe with a beam convergence of 30 mrad (half-angle), whereas collection half-angles of 36 mrad (for high collection efficiency) or 24 mrad (for high energy resolution) were chosen for EELS analysis. The energy loss

spectrometer was set to dispersions of 0.1 or 0.3 eV per channel, depending on the required energy range, resulting in effective energy resolutions (as measured by the full-width at half-maximum of the zero-loss peak) of 0.3 eV or 0.7 eV, respectively (limited by the detector point spread function). Before sample analysis, all FIB lamellae were baked in vacuum for 5 h at 140 °C to remove adsorbed water and contamination from surfaces and provide clean observation conditions. Except for two-dimensional chemical maps, all EEL spectra were collected using distributed dose techniques [smart acquisition (17)], whereby the beam is continuously rastered over areas of interest rather than left stationary for long dwell times, thus further preventing any damage to the specimen and alleviating any issue with EELS fine structure analysis. After each STEM-EELS map or line scan a HAADF image was systematically taken as reference to verify that beam-induced damage on the material was minimal. The spectra were evaluated using Gatan's Digital Micrograph software suite: EEL spectra from regions of interest were extracted by a custom plug-in script (SI Tools) (18), energy-calibrated by setting the onset of the C–K edge to 284 eV, background-subtracted assuming a decaying power-law function, deconvolved for plural scattering with a low-loss spectrum recorded within the same region and the same instrument settings, and smoothed with a low-pass filter in Digital Micrograph to help visualization. Respective energy loss bands were then evaluated and compared with published absorption peaks in the literature (e.g., ref. 19). High-resolution BF and HAADF images were usually recorded by building up image stacks (distributed dose technique), where the beam is scanned repeatedly over the desired field using extremely short dwell times: individual (noisy) frames can then be summed up in later data reduction (20).

1. Busemann H, et al. (2006) Interstellar chemistry recorded in organic matter from primitive meteorites. *Science* 312(5774):727–730.
2. Alexander CMO'D, Fogel M, Yabuta H, Cody GD (2007) The origin and evolution of chondrites recorded in the elemental and isotopic compositions of their macromolecular organic matter. *Geochim Cosmochim Acta* 71(17):4380–4403.
3. Peeters Z, Changela H, Stroud RM, Alexander CMO'D, Nittler LR (2012) Organic carbon inclusions in CR2 chondrite Graves Nunataks 95229. *Meteorit Planet Sci* 47:A312.
4. Pizzarello S, Huang Y, Alexandre MR (2008) Molecular asymmetry in extraterrestrial chemistry: Insights from a pristine meteorite. *Proc Natl Acad Sci USA* 105(10):3700–3704.
5. Leitner J, Vollmer C, Hoppe P, Zipfel J (2012) Characterization of presolar material in the CR chondrite Northwest Africa 852. *Astrophys J* 745(1):38–54.
6. Bradley JP (2003) The astromineralogy of interplanetary dust particles. *Astromineralogy*, ed Henning T (Springer, Berlin), pp 217–235.
7. Nesvorny' D, et al. (2010) Cometary origins of the Zodiacal cloud and carbonaceous micrometeorites. Implications for hot debris disks. *Astrophys J* 713(2):816–836.
8. Floss C, et al. (2004) Carbon and nitrogen isotopic anomalies in an anhydrous interplanetary dust particle. *Science* 303(5662):1355–1358.
9. Messenger S (2000) Identification of molecular-cloud material in interplanetary dust particles. *Nature* 404(6781):968–971.
10. Busemann H, et al. (2009) Ultra-primitive interplanetary dust particles from the comet 26P/Grigg-Skjellerup dust stream collection. *Earth Planet Sci Lett* 288(1-2):44–57.
11. Hoppe P, Cohen S, Meibom A (2013) NanoSIMS: Technical aspects and applications in cosmochemistry and biological geochemistry. *Geostand Geoanalyt Cal Res* 37: 111–154.
12. Marty B, Chaussidon M, Wiens RC, Jurewicz AJG, Burnett DS (2011) A ^{15}N-poor isotopic composition for the solar system as shown by Genesis solar wind samples. *Science* 332(6037):1533–1536.
13. Holzapfel C, Soldera F, Vollmer C, Hoppe P, Mücklich F (2009) TEM foil preparation of sub-um sized grains by the Focused ion beam technique. *J Electron Microsc (Tokyo)* 235(1):59–66.
14. Bassim ND, et al. (2011) Minimizing damage during FIB sample preparation of soft materials. *J Microsc* 245(3):288–301.
15. Malis T, Cheng SC, Egerton RF (1988) EELS log-ratio technique for specimen-thickness measurement in the TEM. *J Electron Microsc Tech* 8(2):193–200.
16. Krivanek OL, et al. (2010) Gentle STEM: ADF imaging and EELS at low primary energies. *Ultramicrosc* 110(8):935–945.
17. Sader K, et al. (2010) Smart acquisition EELS. *Ultramicrosc* 110(8):998–1003.
18. Mitchell DRG, Schaffer B (2005) Scripting-customized microscopy tools for Digital Micrograph. *Ultramicroscopy* 103(4):319–332.
19. De Gregorio BT, et al. (2010) Isotopic anomalies in organic nanoglobules from Comet 81P/Wild 2: Comparison to Murchison nanoglobules and isotopic anomalies induced in terrestrial organics by electron irradiation. *Geochim Cosmochim Acta* 74(15):4454–4470.
20. Buban JP, Ramasse Q, Gipson B, Browning ND, Stahlberg H (2010) High-resolution low-dose scanning transmission electron microscopy. *J Electron Microsc (Tokyo)* 59(2): 103–112.

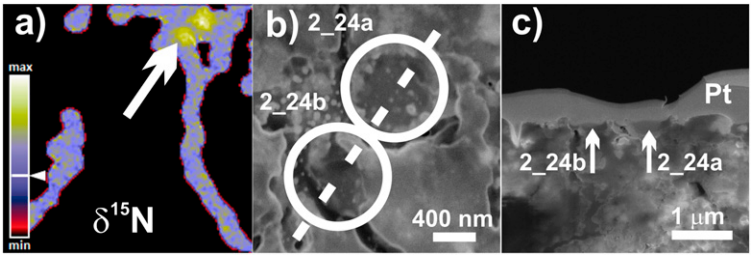

Fig. S1. NanoSIMS and SEM images of anomalous organic grains in the CR chondrite NWA 852. (*A*) NanoSIMS ion ratio image (10 × 10 μm^2) of δ^{15}N in matrix region of NWA grains 2_24a+b (marked by arrow). Black regions represent matrix areas with count rates too low for reliable isotope analysis. (*B*) SEM image of the two grains (encircled) with the orientation of the FIB section shown by the dotted line. (*C*) SEM image of the final FIB section (perpendicular to plane of *A* and *B*) with the Pt strap on top and the two grains marked by arrows.

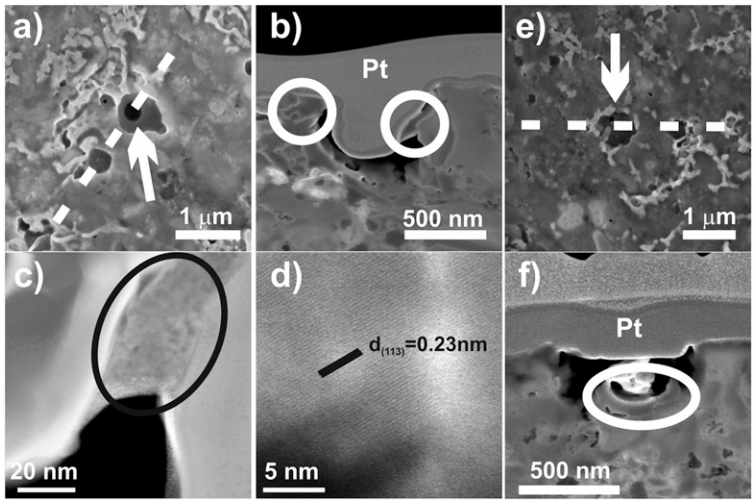

Fig. S2. SEM-UltraSTEM images of organic grains 13_4 and 14_2 from the CR chondrite GRA 95229. (*A*) Grain 13_4 within the matrix (marked by arrow) with the distinct globular morphology and the direction of the FIB section indicated. (*B*) SEM image of the remaining material of grain 13_4 in the final FIB section encircled. The Pt strap is located on top and has filled up the hollow nanoglobular morphology of the grain. (*C*) HAADF overview image of the remaining material of grain 13_4 (encircled) with distinct mottled contrast due to crystalline inclusions. (*D*) HR image of 13_4 with lattice fringes of nanocrystals which can be assigned to calcite d values. (*E*) Grain 14_2 within the matrix (marked by arrow) and the direction of the FIB section indicated. It exhibits a more blocky appearance. (*F*) SEM image of the remaining material of grain 14_2 in the final FIB section encircled.

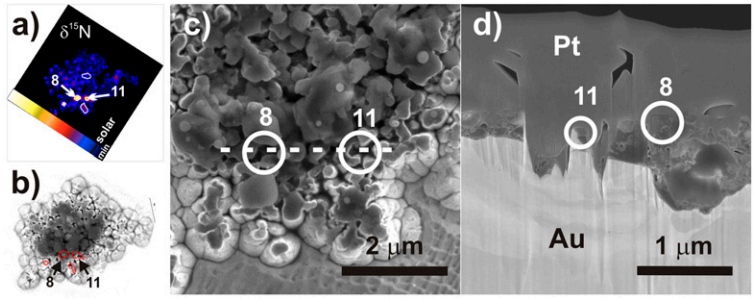

Fig. S3. NanoSIMS and SEM images of organic grains in IDP AK5. (*A*) NanoSIMS ion ratio image (size 10×10 μm^2, rotated to fit orientation of SEM image) of δ^{15}N with grains 08 and 11 (both ^{15}N-enriched) clearly visible above the solar system background (together with some other hot spots within the same particle). (*B*) SEM image of the particle with the outlines of the anomalies put over the image to relocate respective grains. (*C*) Detail SEM image of the particle with grains 8 and 11 encircled and the location of the FIB lamella indicated by a dotted line. (*D*) SEM image of the FIB section with grains 8 and 11 encircled and sandwiched between the Pt cover at the top and the Au substrate at the bottom (reversed view).

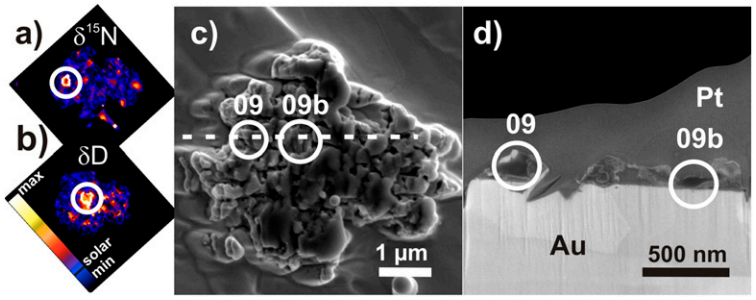

Fig. S4. NanoSIMS and SEM images of organic grains in IDP AK6. (*A* and *B*) NanoSIMS ion ratio images (size 10×10 μm^2 each, rotated to fit orientation of SEM images) of δ^{15}N (*A*) and δD (*B*) in IDP AK6 with color-coded bar. Grains 09 (^{15}N-enriched) and 09b (D-enriched) are clearly visible above the solar system background. (*C*) The approximate location of the two grains within the IDP with the direction of the FIB lamella indicated. (*D*) SEM image of the FIB section with the two grains encircled and sandwiched between the Pt strap at the top and the Au substrate at the bottom.

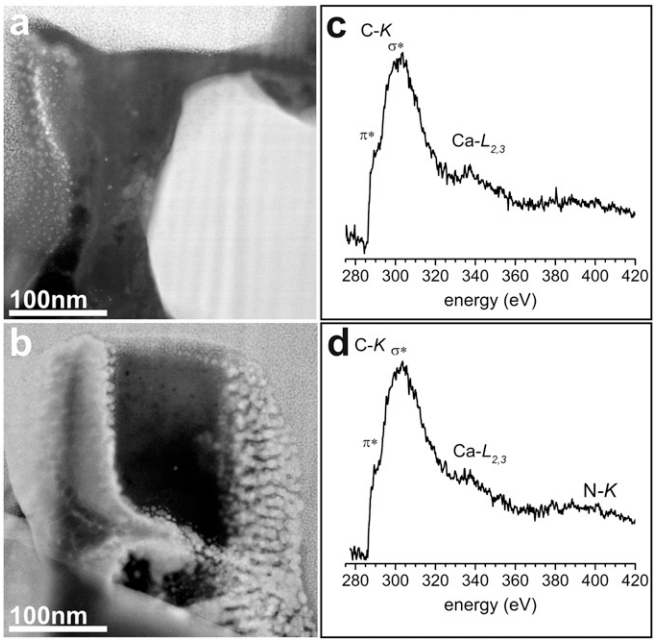

Fig. S5. UltraSTEM images and EEL spectra over the whole energy range of organic grains 8 and 11 from the IDP AK5. (*A*) HAADF overview image of the irregular grain 8. (*B*) HAADF overview image of the blocky grain 11. (*C* and *D*) Extracted EEL spectra of organic grains 8 (*C*) and 11 (*D*) with distinct edges marked. The N–K edge could be detected in grain 11 but is very noisy. The Ca–$L_{2,3}$ lines are visible in EEL spectra from both grains.

Table S1. Overview of identified EELS fine structure and associated functional group chemistry in isotopically anomalous organic grains

Identified energy band, eV	Functional group	Identified in grain no.
Carbon K		
285 (A)	Aromatic C = C	All grains
286.3–286.8 (B)	Aldehyde O = CH Ketone C = O Nitrile C≡N	All grains
287.2–288.3 (C)	Aliphatic C–C	All IDP grains
288.5–288.7 (D)	Carboxyl O = C–O	GRA 95229: grain 14_2
290.3 (E)	Carbonate CO_3	GRA 95229: both grains
Nitrogen K		
398.8/399.7–399.9	Imine C = N/ Nitrile C≡N	NWA 852: grains 2_24a+b GRA 95229: grain 13_4 IDP AK5: grain 11
402.2–402.4	Pyrrole C_4H_4NH	NWA 852: grains 2_24a+b
399.9, 402.3, 406.8, 411.4	Imidazole $C_3H_4N_2$	NWA 852: grains 2_24a+b

Table S2. Overview of isotopic compositions and sizes of isotopically anomalous organic grains

Grain	$\delta^{15}N$, ‰	δD, ‰	$\delta^{13}C$, ‰	Size (SEM), nm	Size (FIB), nm
NWA852_2_24a	430 ± 15	n.m.	20 ± 10	630 × 570	590 × 210
NWA852_2_24b	360 ± 10	n.m.	−10 ± 10	490 × 300	400 × 100
GRA95229_13_4	680 ± 10	n.m.	30 ± 10	760 × 630	190 × 60
GRA95229_14_2	770 ± 30	n.m.	−110 ± 10	690 × 650	390 × 70
IDP AK5 hot spot 08	1200 ± 60	0	30 ± 10	360 × 340	180 × 60
IDP AK5 hot spot 11	1230 ± 90	n.m.	0	440 × 280	80 × 60
IDP AK6 hot spot 09	1520 ± 240	0	0	200 × 190	150 × 150
IDP AK6 hot spot 09b	0	5600 ± 500	10 ± 20	540 × 380	270 × 60

n.m., not measured.